Research Article Vol. 56, No. 30 / October 20 2017 / Applied Optics 8477

applied optics

Methods of polarimetric calibration and reconstruction for a fieldable channeled dispersive imaging spectropolarimeter

Bin Yang,[1,2] Junqiang Zhang,[1,*] Changxiang Yan,[1] and Xueping Ju[1,2]

[1]Changchun Institute of Optics, Fine Mechanics and Physics, Chinese Academy of Sciences, Changchun 130033, China
[2]University of Chinese Academy of Sciences, Beijing 100049, China
*Corresponding author: zhangjqciom@sina.com

Received 5 July 2017; revised 27 August 2017; accepted 19 September 2017; posted 20 September 2017 (Doc. ID 301649); published 19 October 2017

Polarimetric calibration and reconstruction methods for a fieldable channeled dispersive imaging spectropolarimeter (CDISP) are presented. A theoretical model for the polarimetric calibration is derived first. In the polarimetric calibration for the CDISP, the alignment errors of the polarimetric spectral intensity modulation module, and the polarization effects of the optical system and phase factors of the high-order retarders at different viewing angles, are considered and determined independently. Based on the results of the polarimetric calibration, the Stokes vector of the target is reconstructed through the derived reconstruction model. Simulation results with a fieldable CDISP designed for airborne remote sensing indicate that by using the presented polarimetric calibration and reconstruction methods, the measurement accuracy at each viewing angle of the fieldable CDISP can be improved. Experimental results are summarized and analyzed to demonstrate the effectiveness of the presented methods.

OCIS codes: (120.5410) Polarimetry; (110.5405) Polarimetric imaging; (110.4234) Multispectral and hyperspectral imaging.

https://doi.org/10.1364/AO.56.008477

1. INTRODUCTION

An imaging spectropolarimeter can simultaneously measure the spatial, spectral, and polarization data of a target, which combines the abilities of an imaging spectrometer and imaging polarimeter [1,2]. It has been well recognized in many fields, such as remote sensing, material characterization, and biomedical optics [3–7]. However, in conventional imaging spectropolarimeters, the data cube is obtained by scanning in the spatial, spectral, or polarization dimension, where the mechanically movable components and micro-retarder or micro-polarizer arrays generally cause apparatuses to suffer from vibration, heat generation, electrical noise, and alignment difficulty [8,9].

The channeled polarimetric technique, presented by Oka and Kato [10] and Iannarilli *et al.* [11], is capable of measuring the spectra of the four Stokes parameters in a snapshot, which is a preferable candidate for the imaging spectropolarimetry. In recent years, the channeled polarimetric technique has been incorporated into different types of imaging spectrometers, such as the dispersive imaging spectrometer [4,12], Fourier transform imaging spectrometer [1,13], and computed tomography imaging spectrometer [14,15]. Among these combinations, the channeled polarimetric technique working with the dispersive imaging spectrometer has many unique advantages, which can keep good performance with the environmental perturbations, such as vibration, stress, and fluctuations in ambient temperature, etc. Furthermore, the optical system of the channeled dispersive imaging spectropolarimeter (CDISP) is simple and the airborne measurement results indicate that it can be well used in the airborne quantitative remote sensing [12]. Noteworthy is that the CDISP should be calibrated accurately before quantitative-grade applications. Sabatke *et al.* presented an approach to system calibration and target reconstruction for the channeled spectropolarimetry [16]. Jones *et al.* first realized a quantitative-grade, fieldable snapshot dispersive imaging spectropolarimeter [4]. In the above studies, the spectropolarimeter was considered as a linear operator and presented as a matrix. The matrix was estimated in the calibration procedure and pseudoinverted to reconstruct the target. This method could ensure the reconstruction accuracy of the Stokes vector. However, it requires a large amount of experimental data with high accuracy and the data processing is complicated. Taniguchi *et al.* presented self-calibration and reference beam calibration methods for the channeled spectropolarimetry [17]. Using the methods, they could calibrate the phase factors of the high-order retarders accurately. Nevertheless, they did not consider the influences of the

alignment errors of the polarimetric spectral intensity modulation (PSIM) module and polarization effects of the optical system. To the best of our knowledge, the problems of the polarimetric calibration and reconstruction for the fieldable CDISP cannot be well solved with the previous literature.

In this paper, we present practical polarimetric calibration and reconstruction methods for the fieldable CDISP. When performing the polarimetric calibration, the alignment errors of the PSIM module, and the polarization effects of the optical system and phase factors of the high-order retarders at different viewing angles are determined accurately. By using the presented methods, the reconstruction accuracy of the Stokes vector at each viewing angle of the fieldable CDISP can be improved obviously, which is significant for the practical quantitative-grade applications of the fieldable CDISP. In this paper, Section 2 describes the principle of the channeled dispersive imaging spectropolarimetry. Section 3 derives a new theoretical model and presents a method of polarimetric calibration. Section 4 develops a reconstruction method based on the polarimetric calibration results. In Sections 5 and 6, we summarize and analyze the simulation and experimental results, respectively. The conclusion is presented in Section 7.

2. PRINCIPLE OF THE CHANNELED DISPERSIVE IMAGING SPECTROPOLARIMETRY

The optical schematic of the fieldable CDISP is depicted in Fig. 1. We use the fieldable CDISP designed for remote sensing as an example to analyze the presented methods in this paper. Polychromatic light from a target is collected and collimated by the fore-optics, and then passes through the PSIM module, imaging optics, and slit. Finally, it is launched into the dispersive imaging spectrometer. The PSIM module is composed of two high-order retarders, R_1 and R_2, and a polarizer, P. In the fieldable CDISP, for avoiding substantially more complicated propagation behavior in the crystal, all incident angles on the high-order retarders, R_1 and R_2, should be limited to less than about 5° [4]. In order to meet this requirement, the fore-optics is generally used to collimate the light to reduce the incident angles on R_1 and R_2. We use the transmission axis of P as the x-axis, the direction perpendicular to the transmission axis of P as the y-axis, and the optical axis as the z-axis to establish a right-handed coordinate system. The fast axes of R_1 and R_2 are oriented at 0° and 45° relative to the x-axis, respectively. The thickness ratio of R_1 and R_2 is chosen to be 1∶2. The slit is aligned along the direction of the x-axis. In the CDISP, the spectrometer is generally designed based on an Offner relay

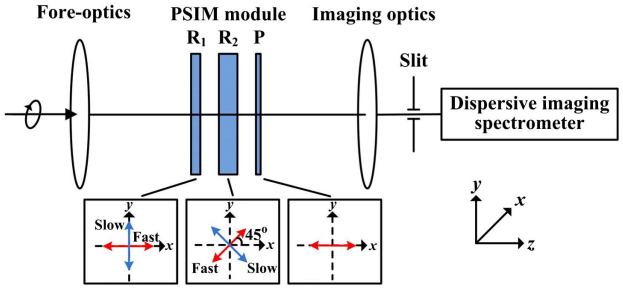

Fig. 1. Optical schematic of the fieldable CDISP.

using a reflective convex grating [4]. The sensor of the spectrometer records spectra along one dimension perpendicular to the slit, and one-dimensional spatial imaging along the other dimension parallel to the slit within a single integration time of the sensor. The two-dimensional spatial imaging of the target can be obtained by scanning the sensor in push-broom mode.

For a channeled non-imaging spectropolarimeter, the polarization effects of the optical system except the PSIM module are generally too small to be ignored. The spectrum obtained by the perfectly aligned channeled non-imaging spectropolarimeter can be expressed as

$$\begin{aligned} B'(\sigma) = {} & (1/2)S_0(\sigma) \\ & + (1/4)|S_{23}(\sigma)|\cos\{\varphi_2(\sigma) - \varphi_1(\sigma) + \arg[S_{23}(\sigma)]\} \\ & - (1/4)|S_{23}(\sigma)|\cos\{\varphi_2(\sigma) + \varphi_1(\sigma) - \arg[S_{23}(\sigma)]\} \\ & + (1/2)|S_1(\sigma)|\cos\{\varphi_2(\sigma) + \arg[S_1(\sigma)]\}, \end{aligned} \tag{1}$$

where σ is the wavenumber, and arg indicates the operator to take the argument. $\varphi_1(\sigma)$ and $\varphi_2(\sigma)$ are the phase factors of R_1 and R_2, respectively. $S_{23}(\sigma) = S_2(\sigma) + iS_3(\sigma)$, and $S_k(\sigma)$, $(k = 0\ldots3)$ denotes the Stokes parameter of the incident light. By performing the inverse Fourier transformation of $B'(\sigma)$, seven separated channels containing different Stokes components are obtained. The desired channels can be extracted by the frequency filtering technique and then performed Fourier transformations to reconstruct the Stokes vector of the incident light [10].

For a fieldable CDISP, the polarization effects of the optical components, such as lens, mirror, and grating, cannot be ignored and they are different at different viewing angles. For example, the diattenuation of the optics of the typical instrument, named polarization and directionality of the Earth's reflectances (POLDER), increases obviously with the viewing angle, and achieves about 5% at the viewing angle of 57.5° [18]. The polarization effects will produce false polarization information to reduce the measurement accuracy of the fieldable CDISP without calibration. Furthermore, the phase factors of the high-order retarders will change with the viewing angle, and the misalignments of the PSIM module are inevitable in a practical application. These influence factors can also introduce measurement errors if they are ignored. By using the classical polarimetric calibration methods for channeled spectropolarimetry, i.e., the reference beam calibration method and self-calibration method [17], we can only calibrate the phase factors of the high-order retarders, which is not enough to ensure the measurement accuracy of the fieldable CDISP after calibration. As a result, to improve the measurement accuracy of the fieldable CDISP, we should explore polarimetric calibration and reconstruction methods considering the alignment errors of the PSIM module, and polarization effects of the optical system and variations of the phase factors of the high-order retarders at different viewing angles.

3. POLARIMETRIC CALIBRATION METHOD

In this section, we present a practical polarimetric calibration method for the fieldable CDISP. Before presenting the method, we derive a theoretical model for the polarimetric calibration.

A. Derivation of Theoretical Model

Generally, the Mueller matrix of a system can be obtained by multiplying the Mueller matrices of all the elements of the system. To simplify the expression for the Mueller matrix of the system, we can first choose the Mueller matrices of several of the elements to multiply to be one Mueller matrix, which is used to describe the characteristics of the chosen elements. Based on this idea, when deriving the theoretical model, we divide the fieldable CDISP into four subsystems, i.e., fore-optics, PSIM module, imaging optics, and dispersive imaging spectrometer, and use one Mueller matrix to describe each subsystem. In the polarimetric calibration, we should focus on determining the Mueller matrix of the entire system, with no need for determining the Mueller matrix of each element. From this perspective, the method used in deriving the theoretical model for the polarimetric calibration is feasible. Furthermore, the researchers determined the polarization rate of the optics of the POLDER instrument according to a similar idea, and the results validated the effectiveness of the modeling approach [18].

We compute the Stokes vector of the target light passing through the system at the viewing angle θ, which is given by

$$\mathbf{S}_{\text{out}}(\sigma,\theta) = \mathbf{M}_{\text{spec}}(\sigma,\theta)\cdot\mathbf{M}_{\text{imag}}(\sigma,\theta)\cdot\mathbf{M}_{\text{PSIM}}(\sigma,\theta)\cdot\mathbf{M}_{\text{fore}}(\sigma,\theta)\cdot\mathbf{S}(\sigma), \tag{2}$$

where $\mathbf{M}_{\text{spec}}$, $\mathbf{M}_{\text{imag}}$, $\mathbf{M}_{\text{PSIM}}$, and $\mathbf{M}_{\text{fore}}$ are the Mueller matrices of the dispersive imaging spectrometer, imaging optics, PSIM module, and fore-optics. Because the Mueller matrices at different viewing angles are different, we use the parameter θ to distinguish the Mueller matrices at different viewing angles.

The dispersive imaging spectrometer is composed of many reflecting interfaces, in which the reflective convex grating can be assumed to be a reflective surface in the polarimetric calibration. Hence, the dispersive imaging spectrometer can be equivalent to be a reflector at each viewing angle. The polarization effects of the reflection at homogenous and isotropic interface include diattenuation and retardance [19]. The equivalent Mueller matrix of the dispersive imaging spectrometer at the viewing angle θ is given by

$$\mathbf{M}_{\text{spec}}(\sigma,\theta) = A_{\text{spec}}(\sigma,\theta)\cdot\begin{bmatrix} 1 & D_{\text{spec}}(\sigma,\theta) & 0 & 0 \\ D_{\text{spec}}(\sigma,\theta) & 1 & 0 & 0 \\ 0 & 0 & -J_{\text{spec},2}(\sigma,\theta) & -J_{\text{spec},1}(\sigma,\theta) \\ 0 & 0 & J_{\text{spec},1}(\sigma,\theta) & -J_{\text{spec},2}(\sigma,\theta) \end{bmatrix}, \tag{3}$$

where $A_{\text{spec}}(\sigma,\theta) = [R^s_{\text{spec}}(\sigma,\theta) + R^p_{\text{spec}}(\sigma,\theta)]/2$, and $R^s_{\text{spec}}(\sigma,\theta)$ and $R^p_{\text{spec}}(\sigma,\theta)$ denote the s-intensity reflectance and p-intensity reflectance of the dispersive imaging spectrometer. $D_{\text{spec}}(\sigma,\theta)$ is the diattenuation, $J_{\text{spec},1}(\sigma,\theta) = \sqrt{1-[D_{\text{spec}}(\sigma,\theta)]^2}\sin[\delta_{\text{spec}}(\sigma,\theta)]$, and $J_{\text{spec},2}(\sigma,\theta) = \sqrt{1-[D_{\text{spec}}(\sigma,\theta)]^2}\cos[\delta_{\text{spec}}(\sigma,\theta)]$, where $\delta_{\text{spec}}(\sigma,\theta)$ denotes the retardance of the dispersive imaging spectrometer. We should mention that $A_{\text{spec}}(\sigma,\theta)$, $D_{\text{spec}}(\sigma,\theta)$, and $\delta_{\text{spec}}(\sigma,\theta)$ will change with the viewing angle. Therefore, they cannot be regarded as constants in the polarimetric calibration.

Similarly, the imaging optics and fore-optics can be equivalent to be a homogenous and isotropic refractor, respectively. The polarization effects of the refraction include diattenuation whether the refracting interface is an uncoated or thin-film coated interface. However, for refraction at an uncoated interface, the retardance is zero, while for a thin-film coated interface, the retardance is nonzero [19]. Since the imaging optics and fore-optics are coated with anti-reflection films, the retardance between the s and p states cannot be ignored. The equivalent Mueller matrices of the imaging optics and fore-optics at the viewing angle θ are expressed as

$$\mathbf{M}_{\text{imag}}(\sigma,\theta) = A_{\text{imag}}(\sigma,\theta)\cdot\begin{bmatrix} 1 & D_{\text{imag}}(\sigma,\theta) & 0 & 0 \\ D_{\text{imag}}(\sigma,\theta) & 1 & 0 & 0 \\ 0 & 0 & J_{\text{imag},2}(\sigma,\theta) & J_{\text{imag},1}(\sigma,\theta) \\ 0 & 0 & -J_{\text{imag},1}(\sigma,\theta) & J_{\text{imag},2}(\sigma,\theta) \end{bmatrix}, \tag{4}$$

$$\mathbf{M}_{\text{fore}}(\sigma,\theta) = A_{\text{fore}}(\sigma,\theta)\cdot\begin{bmatrix} 1 & D_{\text{fore}}(\sigma,\theta) & 0 & 0 \\ D_{\text{fore}}(\sigma,\theta) & 1 & 0 & 0 \\ 0 & 0 & J_{\text{fore},2}(\sigma,\theta) & J_{\text{fore},1}(\sigma,\theta) \\ 0 & 0 & -J_{\text{fore},1}(\sigma,\theta) & J_{\text{fore},2}(\sigma,\theta) \end{bmatrix}, \tag{5}$$

where $A_{\text{imag}}(\sigma,\theta) = [T^s_{\text{imag}}(\sigma,\theta) + T^p_{\text{imag}}(\sigma,\theta)]/2$, and $T^s_{\text{imag}}(\sigma,\theta)$ and $T^p_{\text{imag}}(\sigma,\theta)$ denote the s-intensity transmittance and p-intensity transmittance of the imaging optics, respectively. $D_{\text{imag}}(\sigma,\theta)$ is the diattenuation, $J_{\text{imag},1}(\sigma,\theta) = \sqrt{1-[D_{\text{imag}}(\sigma,\theta)]^2}\sin[\delta_{\text{imag}}(\sigma,\theta)]$, and $J_{\text{imag},2}(\sigma,\theta) = \sqrt{1-[D_{\text{imag}}(\sigma,\theta)]^2}\cos[\delta_{\text{imag}}(\sigma,\theta)]$, where $\delta_{\text{imag}}(\sigma,\theta)$ denotes the retardance of the imaging optics. In Eq. (5), $A_{\text{fore}}(\sigma,\theta) = [T^s_{\text{fore}}(\sigma,\theta) + T^p_{\text{fore}}(\sigma,\theta)]/2$, and $T^s_{\text{fore}}(\sigma,\theta)$ and $T^p_{\text{fore}}(\sigma,\theta)$ denote the s-intensity transmittance and p-intensity transmittance of the fore-optics, respectively. $D_{\text{fore}}(\sigma,\theta)$ is the

diattenuation, $J_{\text{fore},1}(\sigma,\theta)=\sqrt{1-[D_{\text{fore}}(\sigma,\theta)]^2}\sin[\delta_{\text{fore}}(\sigma,\theta)]$, and $J_{\text{fore},2}(\sigma,\theta)=\sqrt{1-[D_{\text{fore}}(\sigma,\theta)]^2}\cos[\delta_{\text{fore}}(\sigma,\theta)]$, where $\delta_{\text{fore}}(\sigma,\theta)$ denotes the retardance of the fore-optics.

Based on the Mueller matrices of the retarder and polarizer [19], we can obtain the Mueller matrix of the PSIM module at the viewing angle θ, which is given by

$$\begin{aligned}&\mathbf{M}_{\text{PSIM}}(\sigma,\theta)\\&=\mathbf{M}_{\text{P}}(0^\circ,\sigma,\theta)\cdot\mathbf{M}_{\text{R2}}[45^\circ+\alpha_2,\varphi_2(\sigma,\theta),\theta]\cdot\mathbf{M}_{\text{R1}}[\alpha_1,\varphi_1(\sigma,\theta),\theta]\\&=A_{\text{PSIM}}(\sigma,\theta)\cdot\begin{bmatrix}1 & m_{12}(\sigma,\theta) & m_{13}(\sigma,\theta) & m_{14}(\sigma,\theta)\\ 1 & m_{22}(\sigma,\theta) & m_{23}(\sigma,\theta) & m_{24}(\sigma,\theta)\\ 0 & 0 & 0 & 0\\ 0 & 0 & 0 & 0\end{bmatrix},\end{aligned}\tag{6}$$

where $\mathbf{M}_{\text{P}}$, $\mathbf{M}_{\text{R2}}$, and $\mathbf{M}_{\text{R1}}$ are the Mueller matrices of the polarizer P, high-order retarder R_2, and high-order retarder R_1, respectively. Because we use the transmission axis of P as the x-axis to establish the coordinate system, α_1 and α_2 indicate the alignment errors of R_1 and R_2, and $\varphi_1(\sigma,\theta)$ and $\varphi_2(\sigma,\theta)$ are the phase factors of R_1 and R_2 at the viewing angle θ. $A_{\text{PSIM}}(\sigma,\theta)$ denotes the intensity transmittance of the PSIM module at the viewing angle θ, and the matrix elements are

$$\begin{aligned}m_{12}(\sigma,\theta)&=m_{22}(\sigma,\theta)\\&=q^2l^2\cos[\varphi_2(\sigma,\theta)]-pl\sin[\varphi_1(\sigma,\theta)]\sin[\varphi_2(\sigma,\theta)],\end{aligned}\tag{7}$$

$$\begin{aligned}m_{13}(\sigma,\theta)&=m_{23}(\sigma,\theta)\\&=-q^2gl\cos[\varphi_1(\sigma,\theta)]+pql^2\cos[\varphi_2(\sigma,\theta)]\\&\quad-(pql^2-q^2gl)\cos[\varphi_1(\sigma,\theta)]\cos[\varphi_2(\sigma,\theta)]\\&\quad+ql\sin[\varphi_1(\sigma,\theta)]\sin[\varphi_2(\sigma,\theta)],\end{aligned}\tag{8}$$

$$\begin{aligned}m_{14}(\sigma,\theta)&=m_{24}(\sigma,\theta)\\&=-qgl\sin[\varphi_1(\sigma,\theta)]-l\cos[\varphi_1(\sigma,\theta)]\sin[\varphi_2(\sigma,\theta)]\\&\quad-(pl^2-qgl)\sin[\varphi_1(\sigma,\theta)]\cos[\varphi_2(\sigma,\theta)],\end{aligned}\tag{9}$$

where $p=\sin(2\alpha_1)$, $q=\cos(2\alpha_1)$, $g=\sin(2\alpha_2)$, and $l=\cos(2\alpha_2)$. Since the alignment errors of the PSIM module are typically small, p and g can be regarded as small quantities. Hence, when deriving the polarimetric calibration model, we ignore the second-order small quantities such as p^2, g^2, and pg.

By multiplying the above matrices according to Eq. (2), we can calculate out the matrix of the system. Then the intensity obtained by the sensor of the spectrometer at the viewing angle θ is given by

$$\begin{aligned}&B(\sigma,\theta)\\&=A(\sigma,\theta)S_0(\sigma)+A(\sigma,\theta)D_{\text{fore}}(\sigma,\theta)S_0(\sigma)\\&\quad-A(\sigma,\theta)\xi_1\sqrt{1-[D_{\text{fore}}(\sigma,\theta)^2]}\\&\quad\cdot[S_2(\sigma)V(\sigma,\theta)+S_3(\sigma)U(\sigma,\theta)]\cos[\varphi_1(\sigma,\theta)]\\&\quad-A(\sigma,\theta)\xi_2\sqrt{1-[D_{\text{fore}}(\sigma,\theta)^2]}\\&\quad\cdot[-S_2(\sigma)U(\sigma,\theta)+S_3(\sigma)V(\sigma,\theta)]\sin[\varphi_1(\sigma,\theta)]\\&\quad+A(\sigma,\theta)\{\xi_3[D_{\text{fore}}(\sigma,\theta)S_0(\sigma)+S_1(\sigma)]+\xi_4\sqrt{1-[D_{\text{fore}}(\sigma,\theta)^2]}\\&\quad\cdot[S_2(\sigma)V(\sigma,\theta)+S_3(\sigma)U(\sigma,\theta)]\}\cos[\varphi_2(\sigma,\theta)]\\&\quad+(1/2)A(\sigma,\theta)\{\xi_5[D_{\text{fore}}(\sigma,\theta)S_0(\sigma)\\&\quad+S_1(\sigma)]-\xi_6\sqrt{1-[D_{\text{fore}}(\sigma,\theta)^2]}\\&\quad\cdot[S_2(\sigma)V(\sigma,\theta)+S_3(\sigma)U(\sigma,\theta)]\}\cos[\varphi_1(\sigma,\theta)+\varphi_2(\sigma,\theta)]\\&\quad-(1/2)A(\sigma,\theta)\xi_7\sqrt{1-[D_{\text{fore}}(\sigma,\theta)^2]}\\&\quad\times[-S_2(\sigma)U(\sigma,\theta)+S_3(\sigma)V(\sigma,\theta)]\\&\quad\cdot\sin[\varphi_1(\sigma,\theta)+\varphi_2(\sigma,\theta)]\\&\quad-(1/2)A(\sigma,\theta)\{\xi_5[D_{\text{fore}}(\sigma,\theta)S_0(\sigma)\\&\quad+S_1(\sigma)]+\xi_8\sqrt{1-[D_{\text{fore}}(\sigma,\theta)^2]}\\&\quad\cdot\{S_2(\sigma)V(\sigma,\theta)+S_3(\sigma)U(\sigma,\theta)\}\}\cos[\varphi_2(\sigma,\theta)-\varphi_1(\sigma,\theta)]\\&\quad+(1/2)A(\sigma,\theta)\xi_9\sqrt{1-[D_{\text{fore}}(\sigma,\theta)^2]}\{-S_2(\sigma)U(\sigma,\theta)\\&\quad+S_3(\sigma)V(\sigma,\theta)\}\cdot\sin[\varphi_2(\sigma,\theta)-\varphi_1(\sigma,\theta)],\end{aligned}\tag{10}$$

where the polarization radiative transfer coefficient of the system, $A(\sigma,\theta)$, is given by

$$\begin{aligned}A(\sigma,\theta)&=\eta(\sigma,\theta)A_{\text{spec}}(\sigma,\theta)A_{\text{imag}}(\sigma,\theta)A_{\text{PSIM}}(\sigma,\theta)A_{\text{fore}}(\sigma,\theta)\\&\quad\cdot[1+D_{\text{spec}}(\sigma,\theta)+D_{\text{imag}}(\sigma,\theta)\\&\quad+D_{\text{spec}}(\sigma,\theta)D_{\text{imag}}(\sigma,\theta)],\end{aligned}\tag{11}$$

where $\eta(\sigma,\theta)$ denotes the response coefficient of the sensor at the viewing angle θ. $U(\sigma,\theta)=\sin[\delta_{\text{fore}}(\sigma,\theta)]$, $V(\sigma,\theta)=\cos[\delta_{\text{fore}}(\sigma,\theta)]$, and ξ_n, $(n=1\ldots9)$ is that

$$\begin{cases}\xi_1=q^2gl & \xi_2=qgl & \xi_3=q^2l^2 & \xi_4=pql^2 & \xi_5=pl\\ \xi_6=(pql^2-qgl+ql) & & \xi_7=(pl^2-qgl+l) & & \\ \xi_8=(pql^2-q^2gl-ql) & & \xi_9=(pl^2-qgl-l) & & \end{cases}.\tag{12}$$

From Eq. (10), we can find that the retardances, $\delta_{\text{imag}}(\sigma,\theta)$ and $\delta_{\text{spec}}(\sigma,\theta)$, will not influence the measurement of the CDISP. Furthermore, the diattenuation magnitudes, $D_{\text{imag}}(\sigma,\theta)$ and $D_{\text{spec}}(\sigma,\theta)$, together become a part of the coefficient $A(\sigma,\theta)$ common to each term in Eq. (10). Therefore, we simply need to determine the shared coefficient $A(\sigma,\theta)$ with no need for determining $D_{\text{imag}}(\sigma,\theta)$ and $D_{\text{spec}}(\sigma,\theta)$ independently in the polarimetric calibration. To calibrate the phase factors, $\varphi_1(\sigma,\theta)$ and $\varphi_2(\sigma,\theta)$, the method for the channeled non-imaging spectropolarimeter is not applicable, because the phase factors may change with the viewing angle and the model becomes more complicated due to $D_{\text{fore}}(\sigma,\theta)$ and $\delta_{\text{fore}}(\sigma,\theta)$. By computing the polarization effects of the

optical system of a fieldable CDISP, whose field of view (FOV) is 40° and F-number is 4, with polarization ray tracing [20–22], we find that the diattenuation of its fore-optics achieves about 0.8% at the edge of the FOV, and the maximum retardance is about 0.03 rad. These polarization effects will influence the measurement accuracy of the fieldable CDISP without calibration. For the CDISP with a wider FOV or smaller F-number, the amplitudes of the diattenuation and retardance may be larger. Therefore, the polarization effects of the fore-optics cannot be ignored in the polarimetric calibration for the fieldable CDISP.

After analysis, we conclude that the fore-optics has more serious effects on the measurement of the CDISP compared with the elements placed in behind of the PSIM module, and the polarization effects of the fore-optics lead to difficulties in the polarimetric calibration. However, we cannot remove the fore-optics or place it in behind of the PSIM module when designing a fieldable CDISP. First, as mentioned above, the fore-optics is generally used to meet the requirement that all incident angles on R_1 and R_2 should be limited to less than about 5° in the fieldable CDISP [4]. Second, without the fore-optics, the diameters of the high-order retarders, R_1 and R_2, and the polarizer P will be larger. But the polarization element with a large diameter is difficult to process. Furthermore, because the thicknesses of R_1 and R_2 are limited, if their diameters are large, the deformations will be inevitable because of the existences of gravity and stress, which seriously influence the performance of the fieldable CDISP. As a result, the fore-optics is essential for the fieldable CDISP, and we need to accurately calibrate the polarization effects of the fore-optics.

The inverse Fourier transformation of $B(\sigma,\theta)$ gives the autocorrelation function, which can be expressed as

$$\begin{aligned} G^{\theta}(h) &= G_0^{\theta}(h) + G_1^{\theta}(h - L_1^{\theta}) + G_1^{\theta *}(-h - L_1^{\theta}) \\ &+ G_2^{\theta}(h - L_2^{\theta}) + G_2^{\theta *}(-h - L_2^{\theta}) \\ &+ G_3^{\theta}[h - (L_1^{\theta} + L_2^{\theta})] + G_3^{\theta *}[-h - (L_1^{\theta} + L_2^{\theta})] \\ &+ G_4^{\theta}[h - (L_2^{\theta} - L_1^{\theta})] + G_4^{\theta *}[-h - (L_2^{\theta} - L_1^{\theta})], \end{aligned} \tag{13}$$

where h is variable conjugate to σ under the Fourier transformation, the superscript θ denotes the viewing angle, and L_1^{θ} and L_2^{θ} denote the optical path differences introduced by R_1 and R_2 at the viewing angle θ in the central wavenumber. The channels are given by

$$G_0^{\theta} = \mathcal{F}^{-1}\{A(\sigma,\theta)[S_0(\sigma) + D_{\text{fore}}(\sigma,\theta)S_1(\sigma)]\}, \tag{14}$$

$$\begin{aligned} G_1^{\theta} = \mathcal{F}^{-1}\{&(1/2)A(\sigma,\theta)\sqrt{1 - [D_{\text{fore}}(\sigma,\theta)]^2} \\ &\cdot \{-S_2(\sigma)[\xi_1 V(\sigma,\theta) + i\xi_2 U(\sigma,\theta)] \\ &+ S_3(\sigma)[-\xi_1 U(\sigma,\theta) + i\xi_2 V(\sigma,\theta)]\} \exp[i\varphi_1(\sigma,\theta)]\}, \end{aligned} \tag{15}$$

$$\begin{aligned} G_2^{\theta} = \mathcal{F}^{-1}\{&(1/2)A(\sigma,\theta)\{\xi_3[D_{\text{fore}}(\sigma,\theta)S_0(\sigma) + S_1(\sigma)] \\ &+ \xi_4\sqrt{1 - [D_{\text{fore}}(\sigma,\theta)^2]}[S_2(\sigma)V(\sigma,\theta) \\ &+ S_3(\sigma)U(\sigma,\theta)]\} \exp[i\varphi_2(\sigma,\theta)]\}, \end{aligned} \tag{16}$$

$$\begin{aligned} G_3^{\theta} = \mathcal{F}^{-1}\{&(1/4)A(\sigma,\theta)\{\xi_5[D_{\text{fore}}(\sigma,\theta)S_0(\sigma) + S_1(\sigma)] \\ &- \sqrt{1 - [D_{\text{fore}}(\sigma,\theta)^2]}S_2(\sigma)[\xi_6 V(\sigma,\theta) + i\xi_7 U(\sigma,\theta)] \\ &- \sqrt{1 - [D_{\text{fore}}(\sigma,\theta)^2]}S_3(\sigma)[\xi_6 V(\sigma,\theta) - i\xi_7 U(\sigma,\theta)]\} \\ &\cdot \exp\{i[\varphi_1(\sigma,\theta) + \varphi_2(\sigma,\theta)]\}\}, \end{aligned} \tag{17}$$

$$\begin{aligned} G_4^{\theta} = \mathcal{F}^{-1}\{&(1/4)A(\sigma,\theta)\{-\xi_5[D_{\text{fore}}(\sigma,\theta)S_0(\sigma) + S_1(\sigma)] \\ &- \sqrt{1 - [D_{\text{fore}}(\sigma,\theta)^2]}S_2(\sigma)[\xi_8 V(\sigma,\theta) - i\xi_9 U(\sigma,\theta)] \\ &- \sqrt{1 - [D_{\text{fore}}(\sigma,\theta)^2]}S_3(\sigma)[\xi_8 V(\sigma,\theta) - i\xi_9 U(\sigma,\theta)]\} \\ &\cdot \exp\{i[\varphi_2(\sigma,\theta) - \varphi_1(\sigma,\theta)]\}\}. \end{aligned} \tag{18}$$

There are nine channels included in $G^{\theta}(h)$. Due to the polarization effects of the fore-optics and alignment errors of the PSIM module, the autocorrelation function becomes more complicated compared with the autocorrelation function of the perfectly aligned channeled non-imaging spectropolarimeter, given in [10]. Two additional channels, centered at $h = \pm L_1^{\theta}$, are introduced into the autocorrelation function. Because the thickness ratio of the two high-order retarders, R_1 and R_2, is designed to be 1:2, the phase factor $\varphi_1(\sigma,\theta)$ is approximately equal to the phase factor $[\varphi_2(\sigma,\theta) - \varphi_1(\sigma,\theta)]$ at each viewing angle. The channels G_1^{θ} and G_4^{θ} are hardly separated from each other over the h domain. As a result, we choose the channels G_0^{θ}, G_2^{θ}, and G_3^{θ}, centered at $h = 0$, L_2^{θ}, and $L_1^{\theta} + L_2^{\theta}$, respectively, in the polarimetric calibration to avoid channel aliasing.

B. Method of Polarimetric Calibration

Based on the derived theoretical model, we present a polarimetric calibration method for the fieldable CDISP. The parameters that need to be calibrated are α_1, α_2, $\exp[i\varphi_1(\sigma,\theta)]$, $\exp[i\varphi_2(\sigma,\theta)]$, $A(\sigma,\theta)$, $D_{\text{fore}}(\sigma,\theta)$, and $\delta_{\text{fore}}(\sigma,\theta)$.

1. Calibration of α_1 and α_2

For the channeled non-imaging spectropolarimeter, we have presented a method which used an auxiliary high-order retarder and a reference beam to calibrate the alignment errors of the PSIM module [23]. Because the alignment errors of the PSIM module do not change with the viewing angle, the previous method we presented remains suitable for the fieldable CDISP. Noteworthy is that the reference beam should pass through the system along the optical axis at the center of the aperture of the system. To meet the above requirement, the incident reference beam is collimated by a collimator and its diameter is reduced by a circular aperture. In this case, the fieldable CDISP can be regarded as the channeled non-imaging spectropolarimeter. We present some of the necessary equations for calibrating the alignment errors of the PSIM module here. The interested reader can find more information in [23].

When calibrating the alignment errors of the PSIM module in [23], we used the slow axis of the auxiliary high-order retarder, R_3, as the x-axis to establish the coordinate system, and θ_1, θ_2, and ε are the alignment errors of R_1, R_2, and P relative to the slow axis of R_3. While in this paper, we use the transmittance axis of P as the x-axis to establish the

coordinate system, and α_1 and α_2 denote the alignment errors of R_1 and R_2 relative to the transmittance axis of P. As a result, the alignment errors in this paper, i.e., α_1 and α_2, can be obtained by coordinate rotating transition,

$$\alpha_1 = \theta_1 - \varepsilon, \tag{19}$$

$$\alpha_2 = \theta_2 - \varepsilon, \tag{20}$$

where θ_1, θ_2, and ε are given by

$$\theta_1 = \frac{1}{2}\arccos\left(\frac{Q}{Q+2N}\right), \tag{21}$$

$$\theta_2 = \frac{1}{2}\arcsin\left[-\frac{W\cos\theta_1}{Q} + \sqrt{\left(\frac{W\cos\theta_1}{Q}\right)^2 - \left(\frac{W}{Q}\right)^2 + \sin^2\theta_1}\right], \tag{22}$$

$$\varepsilon = -\frac{1}{2}\arcsin\left[\sqrt{\frac{(Q\cos\theta_1\sin\theta_2 - H)^2}{Q^2\cos^2\theta_1\cos^2\theta_2 + (Q\cos\theta_1\sin\theta_2 - H)^2}}\right], \tag{23}$$

where

$$\begin{cases} Q = \mathrm{abs}\left[\frac{\mathcal{F}(C_4)}{\mathcal{F}(C_3)}\right] + \mathrm{abs}\left[\frac{\mathcal{F}(C_6)}{\mathcal{F}(C_7)}\right] & N = \mathrm{abs}\left[\frac{\mathcal{F}(C_8)}{\mathcal{F}(C_5)}\right] \\ W = \mathrm{abs}\left[\frac{\mathcal{F}(C_6)}{\mathcal{F}(C_7)}\right] - \mathrm{abs}\left[\frac{\mathcal{F}(C_4)}{\mathcal{F}(C_3)}\right] & H = \mathrm{abs}\left[\frac{\mathcal{F}(C_1)}{\mathcal{F}(C_7)}\right] \end{cases}, \tag{24}$$

where abs stands for the operation of taking the absolute value. C_1, C_3, C_4, C_5, C_6, C_7, and C_8, whose expressions are given by Eqs. (6)–(14) in [23], are the channels of the obtained spectrum when using the auxiliary high-order retarder R_3 to calibrate the alignment errors.

We can add the auxiliary high-order retarder R_3 in front of the fieldable CDISP to calibrate the alignment errors, α_1 and α_2. R_3 will be removed after the calibration of the alignment errors. To avoid the inconvenience that any channel of C_1, C_3, C_4, C_5, C_6, C_7, and C_8, may be zero, the reference beam used here needs to provide that $S_1(\sigma) \neq 0$ and $S_2(\sigma) \neq 0$ or $S_3(\sigma) \neq 0$ [23]. When calibrating the alignment errors, we only use the auxiliary high-order retarder and reference beam to perform one measurement, which does not need a large of measurement data. In addition, the data processing for determining the alignment errors, which includes fast Fourier transformation, frequency filtering, and four-arithmetic operations, is simple and efficient, though the derivation of the theoretical model given in [23] looks complicated.

2. Calibration of $\exp[i\varphi_2(\sigma,\theta)]$

For a fieldable CDISP, the incident angles on the high-order retarders at different viewing angles are different. We should quantitatively study the rule that the phase factor of the high-order retarder changes with the incident angle before the calibration.

The phase factor of the high-order retarder is given by [24]

$$\varphi(\sigma) = 2\pi d\sigma\left\{\sqrt{n_e^2(\sigma) - \left[\frac{n_e^2(\sigma)}{n_o^2(\sigma)}\cos^2\Phi + \sin^2\Phi\right]\sin^2\beta} - \sqrt{n_o^2(\sigma) - \sin^2\beta}\right\}, \tag{25}$$

where d denotes the thickness of the high-order retarder and β is the incident angle on the high-order retarder. $n_o(\sigma)$ is the refractive index of the ordinary ray and $n_e(\sigma)$ is the refractive index of the extraordinary ray. Φ is the relative azimuth angle between the incident plane and the optical axis of the high-order retarder.

From Eq. (25), we can find that the phase factor of the high-order retarder with a fixed thickness is not only related to the state of the incident light (incident and azimuth angles), but also related to the optical axis of the high-order retarder. In the fieldable CDISP, the high-order retarders are generally made of quartz, whose optical axis coincides with its fast axis. Hence, the optical axis of R_2 is oriented at 45° relative to the x-axis. Because the slit of the fieldable CDISP is aligned along the direction of the x-axis, the incident azimuth angles of the light launched into the sensor are approximately equal to 0° relative to the x-axis across the entire FOV. As a result, the value of Φ is about 45° for R_2.

Figure 2 gives the phase factors of R_2 at different incident angles. In the fieldable CDISP, all incident angles on the high-order retarders of the PSIM module should be limited to less than about 5° [4]. We find that the variations of the phase factor of R_2 are less than 1.2×10^{-3} rad with the incident angle changing from 0° to 5°. The influences of these small variations on the measurement accuracy of the fieldable CDISP are too small to be ignored. Therefore, in a fixed wavenumber, $\varphi_2(\sigma,\theta)$ can be supposed to be a constant across the entire FOV.

Based on the above analysis, we can use the value of $\varphi_2(\sigma,\theta)$ at the central FOV as the values of that across the entire FOV in the polarimetric calibration, i.e.,

$$\varphi_2(\sigma,\theta) = \varphi_2^0(\sigma), \tag{26}$$

where the superscript 0 denotes that the light passes through the system along the optical axis at the center of the aperture of the CDISP. Herein, for the high-order retarder, we use the

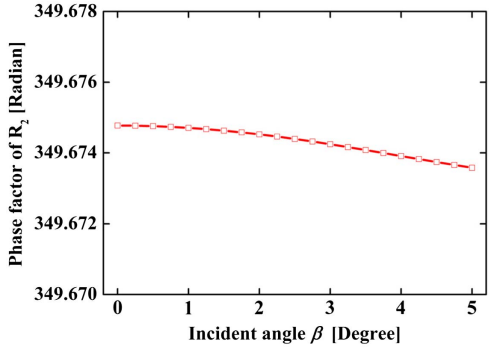

Fig. 2. Phase factors of R_2 at different incident angles. The selected wavenumber is $\sigma = 16969$ cm^{-1}, and the thickness of R_2 is 3.6 mm. The values of $n_o(\sigma)$ and $n_e(\sigma)$ are 1.544 and 1.553 in the selected wavenumber [25].

phase factor of the central FOV chief ray as the phase factor at the central FOV.

To determine $\varphi_2^0(\sigma)$, we shine a 0° linearly polarized reference beam on the system along the optical axis at the center of the aperture. In this way, the beam can be assumed to be normal incident light on the interfaces of the fore-optics. According to Fresnel equations, the polarization effects of the fore-optics can be ignored for the normal incident light, i.e., $D_{\text{fore}}(\sigma, 0) = 0$ and $\delta_{\text{fore}}(\sigma, 0) = 0$ in this case. For the 0° linearly polarized beam, $S_0(\sigma) = S_1(\sigma)$, $S_2(\sigma) = 0$, and $S_3(\sigma) = 0$. Substituting these equations into Eqs. (14), (16), and (17) yields

$$G_{0,0^\circ}^0 = \mathcal{F}^{-1}[A(\sigma, 0)S_0(\sigma)], \tag{27}$$

$$G_{2,0^\circ}^0 = \mathcal{F}^{-1}\{(1/2)A(\sigma, 0)\xi_3 S_1(\sigma)\exp[i\varphi_2^0(\sigma)]\}, \tag{28}$$

$$G_{3,0^\circ}^0 = \mathcal{F}^{-1}\{(1/4)A(\sigma, 0)\xi_5 S_1(\sigma)\exp\{i[\varphi_1^0(\sigma) + \varphi_2^0(\sigma)]\}\}, \tag{29}$$

where $G_{0,0^\circ}^0$, $G_{2,0^\circ}^0$, and $G_{3,0^\circ}^0$ denote the channels obtained when the 0° linearly polarized beam is shined along the optical axis at the center of the aperture of the system, and $\varphi_1^0(\sigma)$ denotes the phase factor introduced by R_1 at the central FOV. By filtering out the desired channels and performing Fourier transformations independently, we can get the expression of $\exp[i\varphi_2^0(\sigma)]$:

$$\exp[i\varphi_2^0(\sigma)] = \frac{2}{\xi_3}\cdot\frac{\mathcal{F}[G_{2,0^\circ}^0]}{\mathcal{F}[G_{0,0^\circ}^0]}. \tag{30}$$

We should mention that we need not to compute $\varphi_2^0(\sigma)$ from $\exp[i\varphi_2^0(\sigma)]$ with a phase unwrapping algorithm, because the phase factor of R_2 is always in the form of $\exp[i\varphi_2(\sigma, \theta)]$ in the polarimetric calibration and reconstruction. ξ_3 can be calculated out using the calibration results of α_1 and α_2. By combining Eqs. (26) and (30), we can determine $\exp[i\varphi_2(\sigma, \theta)]$ for the fieldable CDISP.

3. Calibration of $A(\sigma, \theta)$ and $D_{\text{fore}}(\sigma, \theta)$

For calibrating $A(\sigma, \theta)$ and $D_{\text{fore}}(\sigma, \theta)$, we use an integrating sphere to illuminate the entire FOV of the fieldable CDISP. The light of the integrating sphere can be regarded as unpolarized light, which provides that $S_1(\sigma) = 0$, $S_2(\sigma) = 0$, and $S_3(\sigma) = 0$. According to Eqs. (14) and (16), we can obtain

$$G_{0,u}^\theta = \mathcal{F}^{-1}[A(\sigma, \theta)S_0(\sigma)], \tag{31}$$

$$G_{2,u}^\theta = \mathcal{F}^{-1}\{(1/2)A(\sigma, \theta)\xi_3 D_{\text{fore}}(\sigma, \theta)S_0(\sigma)\exp[i\varphi_2(\sigma, \theta)]\}, \tag{32}$$

where $G_{0,u}^\theta$ and $G_{2,u}^\theta$ denote the channels obtained when the unpolarized light is used to illuminate the entire FOV of the fieldable CDISP. The channels $G_{0,u}^\theta$ and $G_{2,u}^\theta$ are filtered out using the frequency filtering technique and then performed Fourier transformations. Based on them, we can calculate out that

$$A(\sigma, \theta) = \frac{\mathcal{F}(G_{0,u}^\theta)}{S_0(\sigma)}, \tag{33}$$

$$D_{\text{fore}}(\sigma, \theta) = \frac{2}{\xi_3\exp[i\varphi_2(\sigma, \theta)]}\frac{\mathcal{F}(G_{2,u}^\theta)}{\mathcal{F}(G_{0,u}^\theta)}, \tag{34}$$

where $S_0(\sigma)$, the intensity of the light, can be measured by a reference spectroradiometer.

Because $A(\sigma, \theta)$ and $D_{\text{fore}}(\sigma, \theta)$ will change with the viewing angle, we should calibrate them at different viewing angles independently. To improve the efficiency of the polarimetric calibration, we can calibrate $A(\sigma, \theta)$ and $D_{\text{fore}}(\sigma, \theta)$ at part of all the viewing angles, and get the calibration results across the entire FOV through the curve fitting method.

4. Calibration of $\exp[i\varphi_1(\sigma, \theta)]$

We should first analyze the variation of the phase factor of R_1 with the incident angle changing. Because the optical axis of R_1 is oriented at 0° relative to the x-axis, the value of Φ is about 0° for R_1, which is different from that for R_2. According to Eq. (25), we compute the phase factors of R_1 at different incident angles, shown in Fig. 3. The variation of the phase factor of R_1 achieves about 0.3 rad as the incident angle changes from 0° to 5°, which will significantly influence the measurement accuracy of the fieldable CDISP. As a result, $\varphi_1(\sigma, \theta)$ must not be regarded as a constant across the entire FOV.

We present a two-step approach to calibrate $\exp[i\varphi_1(\sigma, \theta)]$. The first step involves determining $\exp[i\varphi_1^0(\sigma)]$, and the second step involves determining $\exp[i\Delta\varphi_1(\sigma, \theta)]$ at different viewing angles, where $\Delta\varphi_1(\sigma, \theta)$ is the additional phase factor of R_1 relative to $\varphi_1^0(\sigma)$ at the viewing angle θ.

To calibrate $\exp[i\varphi_1^0(\sigma)]$, a 45° linearly polarized beam is shined on the system along the optical axis at the center of the aperture. In this case, we conclude that $D_{\text{fore}}(\sigma, 0) = 0$ and $\delta_{\text{fore}}(\sigma, 0) = 0$ according to the above analysis. For the 45° linearly polarized beam, $S_0(\sigma) = S_2(\sigma)$, $S_1(\sigma) = 0$, and $S_3(\sigma) = 0$. Equations (14) and (17) then become

$$G_{0,45^\circ}^0 = \mathcal{F}^{-1}[A(\sigma, 0)S_0(\sigma)], \tag{35}$$

$$G_{3,45^\circ}^0 = \mathcal{F}^{-1}\{-(1/4)A(\sigma, 0)\xi_6 S_2(\sigma)\exp\{i[\varphi_1^0(\sigma) + \varphi_2^0(\sigma)]\}\}, \tag{36}$$

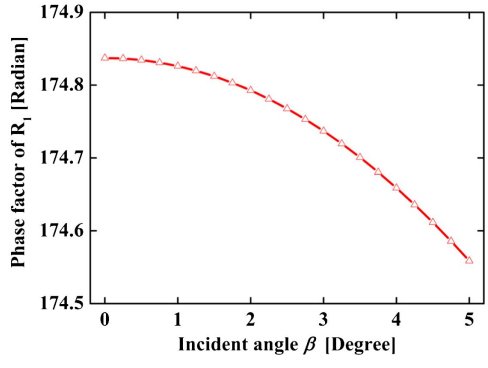

Fig. 3. Phase factors of R_1 at different incident angles in the selected wavenumber of $\sigma = 16969\ \text{cm}^{-1}$. The thickness of R_1 is 1.8 mm.

where $G^0_{0,45^\circ}$ and $G^0_{3,45^\circ}$ denote the channels obtained when the 45° linearly polarized beam is shined along the optical axis at the center of the aperture of the system. Combining Eqs. (35) and (36) and simplifying yields the expression of $\exp[i\varphi_1^0(\sigma)]$ as follows:

$$\exp[i\varphi_1^0(\sigma)] = -\frac{4}{\xi_6 \exp[i\varphi_2^0(\sigma)]} \cdot \frac{\mathcal{F}[G^0_{3,45^\circ}]}{\mathcal{F}[G^0_{0,45^\circ}]}. \tag{37}$$

After determining $\exp[i\varphi_1^0(\sigma)]$, we use the 0° linearly polarized beam as the reference light source to calibrate $\exp[i\Delta\varphi_1(\sigma,\theta)]$ at different viewing angles. During this process, for the abnormal incident light, the polarization effects of the fore-optics can no longer be ignored. Substituting the equations $S_0(\sigma) = S_1(\sigma)$, $S_2(\sigma) = 0$, and $S_3(\sigma) = 0$ into Eq. (17) yields

$$G^\theta_{3,0^\circ} = \mathcal{F}^{-1}\{(1/4)A(\sigma,\theta)\xi_5[D_{\text{fore}}(\sigma,\theta)S_0(\sigma) + S_1(\sigma)] \cdot \exp\{i[\varphi_1(\sigma,\theta) + \varphi_2(\sigma,\theta)]\}\}, \tag{38}$$

where $\varphi_1(\sigma,\theta) = \varphi_1^0(\sigma) + \Delta\varphi_1(\sigma,\theta)$. By combining Eqs. (26), (29), and (38), $\exp[i\Delta\varphi_1(\sigma,\theta)]$ can be expressed as

$$\exp[i\Delta\varphi_1(\sigma,\theta)] = \frac{A(\sigma,0)}{A(\sigma,\theta)[1 + D_{\text{fore}}(\sigma,\theta)]} \cdot \frac{\mathcal{F}[G^\theta_{3,0^\circ}]}{\mathcal{F}[G^0_{3,0^\circ}]}, \tag{39}$$

where $A(\sigma,0)$ can be computed by Eq. (27) with the known incident light intensity measured by the reference spectroradiometer, and $A(\sigma,\theta)$ and $D_{\text{fore}}(\sigma,\theta)$ have been computed in Section 3.B.3. According to $\exp[i\varphi_1(\sigma,\theta)] = \exp[i\varphi_1^0(\sigma)] \cdot \exp[i\Delta\varphi_1(\sigma,\theta)]$, we can determine the exact values of $\exp[i\varphi_1(\sigma,\theta)]$ at different viewing angles.

5. Calibration of $\delta_{\text{fore}}(\sigma,\theta)$

For the fieldable CDISP, the fore-optics is generally composed of many thin-film coated lenses, and the incident angles on the interfaces are relatively large. Therefore, $\delta_{\text{fore}}(\sigma,\theta)$ cannot be ignored across the entire FOV in the polarimetric calibration. When calibrating $\delta_{\text{fore}}(\sigma,\theta)$ at different viewing angles, the 45° linearly polarized beam is used as the reference light source, which provides $S_0(\sigma) = S_2(\sigma)$, $S_1(\sigma) = 0$, and $S_3(\sigma) = 0$. Based on Eqs. (14) and (17), the expressions of $G^\theta_{0,45^\circ}$ and $G^\theta_{3,45^\circ}$ are given by

$$G^\theta_{0,45^\circ} = \mathcal{F}^{-1}[A(\sigma,\theta)S_0(\sigma)], \tag{40}$$

$$G^\theta_{3,45^\circ} = \mathcal{F}^{-1}\{(1/4)A(\sigma,\theta)\{\xi_5 D_{\text{fore}}(\sigma,\theta)S_0(\sigma) - \sqrt{1 - [D_{\text{fore}}(\sigma,\theta)^2]}S_2(\sigma)[\xi_6 V(\sigma,\theta) + i\xi_7 U(\sigma,\theta)]\} \cdot \exp\{i[\varphi_1(\sigma,\theta) + \varphi_2(\sigma,\theta)]\}\}. \tag{41}$$

The channels $G^\theta_{0,45^\circ}$ and $G^\theta_{3,45^\circ}$ are extracted by the frequency filtering technique and performed Fourier transformations independently. Then, we can obtain the expression of $U(\sigma,\theta)$:

$$U(\sigma,\theta) = -\frac{4}{\xi_7\sqrt{1 - [D_{\text{fore}}(\sigma,\theta)]^2}} \cdot \text{Im}\left\{\frac{\mathcal{F}[G^\theta_{3,45^\circ}]}{\mathcal{F}[G^\theta_{0,45^\circ}]\exp\{i[\varphi_1(\sigma,\theta) + \varphi_2(\sigma,\theta)]\}}\right\}, \tag{42}$$

where Im means the operator to take the imaginary part, and $\exp\{i[\varphi_1(\sigma,\theta) + \varphi_2(\sigma,\theta)]\}$ is computed using the calibration results of $\exp[i\varphi_1(\sigma,\theta)]$ and $\exp[i\varphi_2(\sigma,\theta)]$. Because the absolute values of $\delta_{\text{fore}}(\sigma,\theta)$ are much less than π at all the viewing angles, we can obtain the calibration results of $\delta_{\text{fore}}(\sigma,\theta)$ according to the equation $\delta_{\text{fore}}(\sigma,\theta) = \arcsin[U(\sigma,\theta)]$.

After describing the presented polarimetric calibration method, we should discuss a special condition that $\alpha_1 = 0$. Because $\xi_4 = 0$, $\xi_5 = 0$, and $\xi_6 = \xi_7$ when $\alpha_1 = 0$, we can simplify Eqs. (14), (16), and (17):

$$G^\theta_{0,\alpha=0} = \mathcal{F}^{-1}\{A(\sigma,\theta)[S_0(\sigma) + D_{\text{fore}}(\sigma,\theta)S_1(\sigma)]\}, \tag{43}$$

$$G^\theta_{2,\alpha=0} = \mathcal{F}^{-1}\{(1/2)A(\sigma,\theta)\xi_3[D_{\text{fore}}(\sigma,\theta)S_0(\sigma) + S_1(\sigma)] \cdot \exp[i\varphi_2(\sigma,\theta)]\}, \tag{44}$$

$$G^\theta_{3,\alpha=0} = \mathcal{F}^{-1}\{-(1/4)\xi_6 A(\sigma,\theta)S^*_{23}(\sigma) \cdot \exp\{i[\varphi_1(\sigma,\theta) + \varphi_2(\sigma,\theta) + \delta_{\text{fore}}(\sigma,\theta)]\}\}, \tag{45}$$

where $S^*_{23}(\sigma) = S_2(\sigma) - iS_3(\sigma)$. We find that the methods to calibrate α_1, α_2, $\exp[i\varphi_2(\sigma,\theta)]$, $A(\sigma,\theta)$, and $D_{\text{fore}}(\sigma,\theta)$ are not influenced, while the method to calibrate $\exp[i\varphi_1(\sigma,\theta)]$ is not applicable because the channel $G^\theta_{3,0^\circ}$ described by Eq. (38) disappears in this special condition. Hence, if the calibration results of the alignment errors indicate that α_1 is about zero, instead of using the methods given in Sections 3.B.4 and 3.B.5 to determine $\exp[i\varphi_1(\sigma,\theta)]$ and $\delta_{\text{fore}}(\sigma,\theta)$ independently, we use the 45° linearly polarized beam as the reference light source to calibrate $\exp\{i[\varphi_1(\sigma,\theta) + \delta_{\text{fore}}(\sigma,\theta)]\}$. On the basis of Eqs. (43) and (45), we can obtain the calibration result, which is given by

$$\exp\{i[\varphi_1(\sigma,\theta) + \delta_{\text{fore}}(\sigma,\theta)]\} = -\frac{4}{\xi_6 \exp[i\varphi_2(\sigma,\theta)]} \cdot \frac{\mathcal{F}[G^\theta_{3,\alpha=0,45^\circ}]}{\mathcal{F}[G^\theta_{0,\alpha=0,45^\circ}]}. \tag{46}$$

In the presented method, the alignment errors, and the polarization effects of the optical system and phase factors of the high-order retarders at different viewing angles are calibrated. The method uses the three kinds of polarized light with different polarization states, unpolarized light, and an auxiliary high-order retarder to perform the polarimetric calibration. Based on the measurement data for the polarimetric calibration, we can quickly solve the parameters that need to be calibrated according to the presented data processing method.

4. STOKES VECTOR RECONSTRUCTION METHOD

Because of the alignment errors, polarization effects, and variations of the phase factors, the reconstruction errors of the Stokes vector will be introduced if we use the traditional method, named the "reference beam calibration technique," for the channeled non-imaging spectropolarimeter [17]. To improve the reconstruction accuracy of the Stokes vector of the target, we present a new reconstruction method for the fieldable CDISP on the basis of the polarimetric calibration results.

In the Stokes vector reconstruction method, we still use the channels G_0^θ, G_2^θ, and G_3^θ to avoid channel aliasing. After extracting the desired channels of the autocorrelation function, given by Eq. (13), and performing the Fourier transformations independently, we can obtain

$$\mathcal{F}(G_0^\theta) = A(\sigma,\theta)[S_0(\sigma) + D_{\text{fore}}(\sigma,\theta)S_1(\sigma)], \tag{47}$$

$$\begin{aligned}\mathcal{F}(G_2^\theta) = (1/2)A(\sigma,\theta)\{&\xi_3[D_{\text{fore}}(\sigma,\theta)S_0(\sigma) + S_1(\sigma)] \\ &+ \xi_4\sqrt{1-[D_{\text{fore}}(\sigma,\theta)^2]}[S_2(\sigma)V(\sigma,\theta) \\ &+ S_3(\sigma)U(\sigma,\theta)]\}\exp[i\varphi_2(\sigma,\theta)],\end{aligned} \tag{48}$$

$$\begin{aligned}\mathcal{F}(G_3^\theta) = (1/4)A(\sigma,\theta)\{&\xi_5[D_{\text{fore}}(\sigma,\theta)S_0(\sigma) + S_1(\sigma)] \\ &- \sqrt{1-[D_{\text{fore}}(\sigma,\theta)^2]}S_2(\sigma)[\xi_6 V(\sigma,\theta) \\ &+ i\xi_7 U(\sigma,\theta)] \\ &- \sqrt{1-[D_{\text{fore}}(\sigma,\theta)^2]}S_3(\sigma)[\xi_6 V(\sigma,\theta) \\ &- i\xi_7 U(\sigma,\theta)]\}\cdot\exp\{i[\varphi_1(\sigma,\theta)+\varphi_2(\sigma,\theta)]\}.\end{aligned} \tag{49}$$

Combining Eqs. (47)–(49) and simplifying gives the reconstructed Stokes vector of the target light, which is given by

$$S_0(\sigma,\theta) = \frac{Q_3(\sigma,\theta) - Q_4(\sigma,\theta)D_{\text{fore}}(\sigma,\theta)}{1-[D_{\text{fore}}(\sigma,\theta)]^2}, \tag{50}$$

$$S_1(\sigma,\theta) = \frac{Q_4(\sigma,\theta) - Q_3(\sigma,\theta)D_{\text{fore}}(\sigma,\theta)}{1-[D_{\text{fore}}(\sigma,\theta)]^2}, \tag{51}$$

$$S_2(\sigma,\theta) = Q_1(\sigma,\theta)V(\sigma,\theta) + Q_2(\sigma,\theta)U(\sigma,\theta), \tag{52}$$

$$S_3(\sigma,\theta) = Q_1(\sigma,\theta)U(\sigma,\theta) - Q_2(\sigma,\theta)V(\sigma,\theta), \tag{53}$$

where

$$\begin{aligned}Q_1(\sigma,\theta) = &\frac{2\xi_5\mathcal{F}(G_2^\theta)}{(\xi_3\xi_6+\xi_4\xi_5)A(\sigma,\theta)\sqrt{1-[D_{\text{fore}}(\sigma,\theta)^2]}\exp[i\varphi_2(\sigma,\theta)]} \\ &-\frac{4\xi_3\cdot\text{Re}\{\mathcal{F}(G_3^\theta)/\exp\{i[\varphi_1(\sigma,\theta)+\varphi_2(\sigma,\theta)]\}\}}{(\xi_3\xi_6+\xi_4\xi_5)A(\sigma,\theta)\sqrt{1-[D_{\text{fore}}(\sigma,\theta)^2]}}\end{aligned} \tag{54}$$

$$Q_2(\sigma,\theta) = -\frac{4\,\text{Im}\{\mathcal{F}(G_3^\theta)/\exp\{i[\varphi_1(\sigma,\theta)+\varphi_2(\sigma,\theta)]\}\}}{\xi_7 A(\sigma,\theta)\sqrt{1-[D_{\text{fore}}(\sigma,\theta)^2]}}, \tag{55}$$

$$Q_3(\sigma,\theta) = \frac{\mathcal{F}(G_0^\theta)}{A(\sigma,\theta)}, \tag{56}$$

$$\begin{aligned}Q_4(\sigma,\theta) = &\frac{2\mathcal{F}(G_2^\theta)}{\xi_3 A(\sigma,\theta)\exp[i\varphi_2(\sigma,\theta)]} - \frac{\xi_4\sqrt{1-[D_{\text{fore}}(\sigma,\theta)^2]}}{\xi_3} \\ &\cdot\{Q_1(\sigma,\theta) \\ &+ [Q_1(\sigma,\theta) - Q_2(\sigma,\theta)]U(\sigma,\theta)V(\sigma,\theta)\},\end{aligned} \tag{57}$$

where Re denotes the operator to take the real part. The coefficients about the alignment errors in the denominators such as ξ_3, ξ_7, and $(\xi_3\xi_6 + \xi_4\xi_5)$ are always non-zero.

When reconstructing the Stokes vector of the target, we also need to discuss the special condition that $\alpha_1 = 0$. If the calibration results of the alignment errors indicate that α_1 is about zero, the reconstruction model of the Stokes vector would be expressed as

$$S_0(\sigma,\theta) = \frac{\mathcal{F}(G_0^\theta) - 2D_{\text{fore}}(\sigma,\theta)\mathcal{F}(G_2^\theta)/\{\xi_3\exp[i\varphi_2(\sigma,\theta)]\}}{A(\sigma,\theta)\{1-[D_{\text{fore}}(\sigma,\theta)]^2\}}, \tag{58}$$

$$S_1(\sigma,\theta) = \frac{2\mathcal{F}(G_2^\theta)/\{\xi_3\exp[i\varphi_2(\sigma,\theta)]\} - D_{\text{fore}}(\sigma,\theta)\mathcal{F}(G_0^\theta)}{A(\sigma,\theta)\{1-[D_{\text{fore}}(\sigma,\theta)]^2\}}, \tag{59}$$

$$S_2(\sigma,\theta) = \text{Re}\left\{\frac{-4\mathcal{F}(G_3^\theta)}{\xi_6 A(\sigma,\theta)\exp\{i[\varphi_1(\sigma,\theta)+\varphi_2(\sigma,\theta)+\delta_{\text{fore}}(\sigma,\theta)]\}}\right\}, \tag{60}$$

$$S_3(\sigma,\theta) = \text{Im}\left\{\frac{4\mathcal{F}(G_3^\theta)}{\xi_6 A(\sigma,\theta)\exp\{i[\varphi_1(\sigma,\theta)+\varphi_2(\sigma,\theta)+\delta_{\text{fore}}(\sigma,\theta)]\}}\right\}. \tag{61}$$

Since the alignment errors, and the polarization effects and phase factors at different viewing angles are considered in the presented reconstruction method, the reconstructed Stokes vector will be more accurate. Though the form of the derived model becomes more complex compared with the traditional model for the channeled non-imaging spectropolarimeter [10], the added parts contain only the simple trigonometric functions and four-arithmetic operations, which will not lead to difficulties in the reconstruction of the Stokes vector.

5. SIMULATION ANALYSIS

To demonstrate the effectiveness and advantages of the presented methods, simulations for polarimetric calibration and reconstruction are performed. In the simulations, we simulate the polarimetric calibration and target reconstruction with a fieldable CDISP designed for airborne remote sensing in

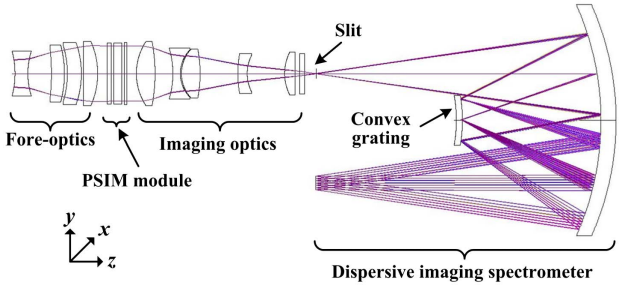

Fig. 4. Schematic layout of the fieldable CDISP.

advance. Figure 4 shows the schematic layout of the fieldable CDISP, which operates over 480–880 nm (11, 364–20, 833 cm^{-1}). The FOV is 40° and the F-number is 4. The radii, thicknesses, and materials of the lenses of the fore-optics and imaging optics are listed in Table 1. The lenses are coated with the anti-reflective films which we design. The radius of the mirror of the imaging spectrometer is −121.56 mm, and the mirror is coated with the aluminum film. R_1 and R_2 are made of quartz. The thicknesses of R_1 and R_2 are 1.8 mm and 3.6 mm, respectively. In the simulations, the dispersion of birefringence of quartz is considered and the reference birefringence at different wavelengths can be found in [25]. The maximum incident angle on R_1 and R_2 is 4.58° in the working wave band, which meets the requirement of less than 5°. Before the polarimetric calibration and reconstruction, we analyze the polarization effects of each part of the optical system through polarization ray tracing [20–22] and compute the phase factors of R_1 and R_2 at different viewing angles by using Eq. (25). Then, the obtained results are used as the input values of the simulations.

We first calibrate the alignment errors of the PSIM module. The input alignment errors of R_1 and R_2 are $\alpha_1 = 0.5°$ and $\alpha_2 = 0.5°$, respectively. Because the alignment errors do not vary with wavenumber, we use the averages of the calculated values of α_1 and α_2 over the working wave band as the calibration results, which are 0.532° and 0.545°. The calibration errors of α_1 and α_2 are less than 0.05°. The results indicate that the presented alignment errors calibration method is appropriate for the fieldable CDISP. However, the precondition is that the reference beam should be shined on the system along the optical axis at the center of the aperture of the fieldable CDISP. The effectiveness of the method for alignment errors calibration has been validated by laboratory experiments [23].

Table 1. Radii, Thicknesses, and Materials of the Lenses

Lens	Radius 1 (mm)	Radius 2 (mm)	Thickness (mm)	Glass in the Schott Catalog
1	−38.07	31.75	5.52	N-SF14
2	−101.80	−46.69	5.59	N-SF66
3	−41.64	−40.01	6.02	SF5
4	−622.95	−34.06	6.00	N-FK56
5	25.21	−73.95	8.00	N-PK52A
6	−38.37	14.78	3.20	KZFS14
7	15.46	−55.97	8.00	N-PK52A
8	50.31	17.30	4.00	SF15
9	20.40	−585.23	4.50	N-PK52A
10	Infinity	Infinity	2.00	F-SILICA

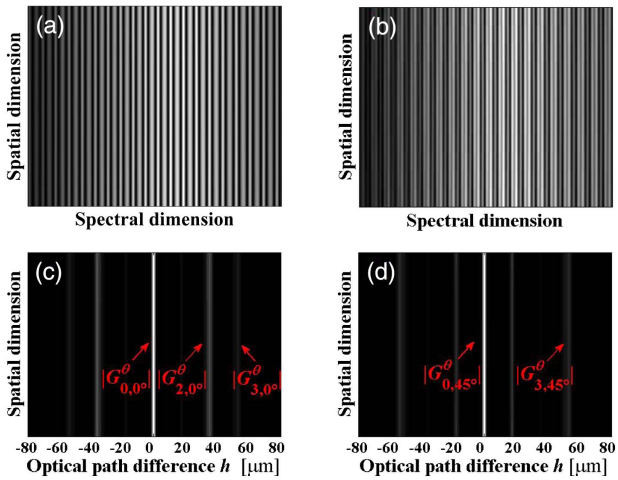

Fig. 5. Intensity images and magnitudes of their autocorrelation functions when the 0° and 45° linearly polarized reference beams are shined on the system. The intensity images of the (a) 0° and (b) 45° linearly polarized reference beams; the magnitudes of the autocorrelation functions of the (c) 0° and (d) 45° linearly polarized reference beams.

As described in Section 3, the presented method determines the parameters at different viewing angles based on the intensities obtained by the sensor and magnitudes of their autocorrelation functions, when the reference polarized light is shined on the system. In this paper, we provide the obtained intensity images and magnitudes of the autocorrelation functions of the 0° and 45° linearly polarized reference beams, which are shown in Fig. 5. In the simulations, the beams are set to be uniform in space distribution. It is apparent that the intensity images and their autocorrelation functions are different under the incident light with different polarization states. We find that the intensities are modulated with the phase factors of the high-order retarders. The autocorrelation functions are obtained by the inverse Fourier transformations of the corresponding intensity images. In Figs. 5(c) and 5(d), the light fringes denote the channels, and the desired channels, $G^{\theta}_{0,0°}$, $G^{\theta}_{2,0°}$, $G^{\theta}_{3,0°}$, $G^{\theta}_{0,45°}$, and $G^{\theta}_{3,45°}$, are separated from one another over the h axis, which is consistent with the theoretical analysis. According to the presented polarimetric calibration method, the desired channels are extracted by the frequency filtering technique and performed Fourier transformations independently to determine the parameters. We should mention that the intensity of the channel $G^{\theta}_{3,0°}$ is relatively weak, which is because its coefficient includes a small amount, ξ_5. However, Eq. (39) shows that ξ_5 is divided out through the operation $\mathcal{F}[G^{\theta}_{3,0°}]/\mathcal{F}[G^{0}_{3,0°}]$ when we use the channel $G^{\theta}_{3,0°}$. Hence, the relatively weak intensity of $G^{\theta}_{3,0°}$ does not influence the polarimetric calibration.

Figure 6 shows the input values and calibration results of $\varphi_1(\sigma, \theta)$ and $\varphi_2(\sigma, \theta)$. We take the results in the central wavenumber at 21 sampled viewing angles as examples to demonstrate the effectiveness of the presented method. To better analyze the calibration results, we compute $\varphi_1(\sigma, \theta)$ and

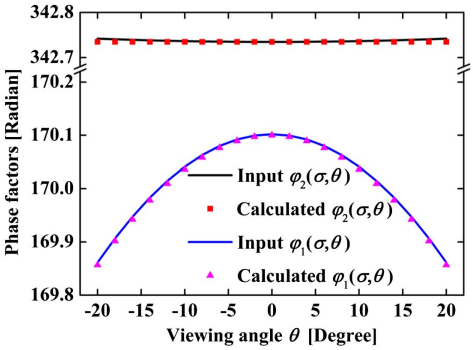

Fig. 6. Input values and calibration results of $\varphi_1(\sigma,\theta)$ and $\varphi_2(\sigma,\theta)$ in the central wavenumber at different viewing angles. The central wavenumber is 16, 098 cm^{-1}.

$\varphi_2(\sigma,\theta)$ from $\exp[i\varphi_1(\sigma,\theta)]$ and $\exp[i\varphi_2(\sigma,\theta)]$ using a phase unwrapping algorithm, though it is not needed in the polarimetric calibration and reconstruction. We find that $\varphi_1(\sigma,\theta)$ changes obviously with the viewing angle while the variation of $\varphi_2(\sigma,\theta)$ is small, which is consistent with the above analysis. The calibration errors of $\varphi_1(\sigma,\theta)$ are 2.1×10^{-3} rad at the central FOV and 4.8×10^{-3} rad at the edge of the FOV, which increase slowly with the viewing angle increasing. We think the reason is that the polarization effects of the fore-optics are more obvious at the larger viewing angle. We have calibrated the polarization effects by the presented method. However, the residual errors of the polarization effects are inevitable and they are relatively large at the larger viewing angle, which will influence the calibration of $\varphi_1(\sigma,\theta)$. When calibrating $\varphi_2(\sigma,\theta)$, we use the value at the central FOV as the calibration result across the entire FOV. Therefore, the calibration error of $\varphi_2(\sigma,\theta)$ is also relatively large at the edge of the FOV, which is about 5.4×10^{-3} rad. The errors of the calibration results of $\varphi_1(\sigma,\theta)$ and $\varphi_2(\sigma,\theta)$ are less than 5.4×10^{-3} rad across the entire FOV, which can be ignored in the Stokes vector reconstruction. After analysis, we conclude that the phase factors of the high-order retarders at different viewing angles can be determined accurately by the presented polarimetric calibration method.

The input values and calibration results of $A(\sigma,\theta)$ at different viewing angles are shown in Fig. 7. In the simulations,

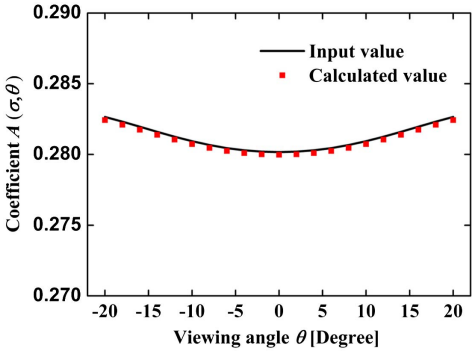

Fig. 7. Input values and calibration results of $A(\sigma,\theta)$ in the central wavenumber at different viewing angles.

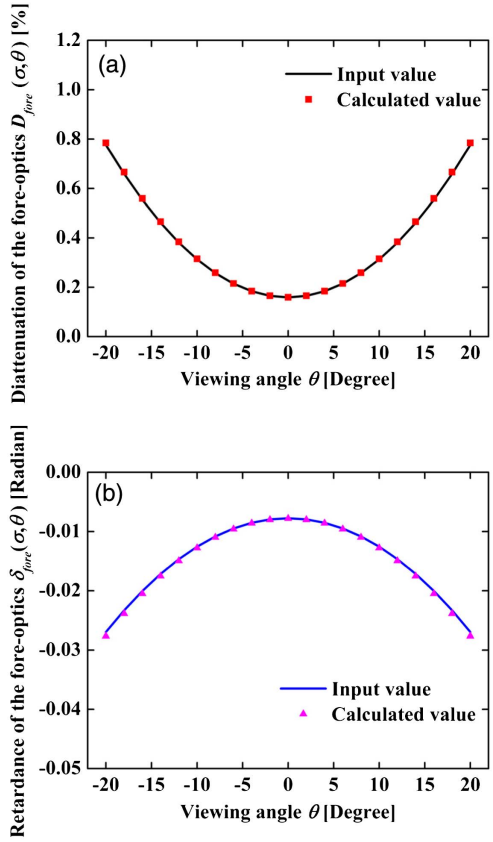

Fig. 8. Input values and calibration results of the polarization effects of the fore-optics (a) $D_{\text{fore}}(\sigma,\theta)$ and (b) $\delta_{\text{fore}}(\sigma,\theta)$ in the central wavenumber at different viewing angles.

we suppose that the response coefficients of the sensor are $\eta(\sigma,\theta)=1$ for all the pixels over the working wave band, which does not affect the discussion about the presented method. The relative errors of the calibration results of $A(\sigma,\theta)$ are less than 0.1% at all the viewing angles. The results with high accuracy are attributed to the fact that only the channel $G^{\theta}_{0,u}$ of the autocorrelation function is used, which will not be influenced by the calibration errors of the polarization effects and phase factors.

Figure 8 gives the input values and calibration results of the polarization effects, including the diattenuation and retardance, of the fore-optics at different viewing angles. Noteworthy is that the polarization effects at the central FOV are non-zero, because the light at the edge of the aperture cannot be assumed to be normal incident light. This is why we emphasize that, to avoid the polarization effects of the fore-optics in some steps of the polarimetric calibration, the beam should be shined on the system along the optical axis at the center of the aperture. At the edge of the FOV, the magnitudes of the diattenuation and retardance are about 0.8% and 0.03 rad, respectively, which will seriously affect the measurement accuracy of the fieldable CDISP if they are ignored in the polarimetric calibration and reconstruction. From the results, we find that with the viewing angle increasing, the polarization effects of the fore-optics become more obvious, and the residual errors of the polarization effects after calibration become larger, which validates

the above analysis of the calibration errors of $\varphi_1(\sigma,\theta)$. The difficulty of the polarimetric calibration for the fieldable CDISP is that the polarization effects and variable phase factors are coupled at each viewing angle. In the presented method, the polarization effects and phase factors at different viewing angles are analyzed and calibrated independently, which is helpful to improve the accuracy of the polarimetric calibration. The maximum residual errors of $D_{\text{fore}}(\sigma,\theta)$ and $\delta_{\text{fore}}(\sigma,\theta)$ are less than 0.02% and 1.0×10^{-3} rad, respectively. The accurate results show that the influences of the polarization effects on the measurement of the fieldable CDISP can be reduced effectively.

From the above calibration results, we find that $\varphi_1(\sigma,\theta)$, $A(\sigma,\theta)$, $D_{\text{fore}}(\sigma,\theta)$, and $\delta_{\text{fore}}(\sigma,\theta)$ change with the viewing angle obviously, and they should be calibrated at each viewing angle. While for $\varphi_2(\sigma,\theta)$, we only need to determine the value at the central FOV. On the basis of the calibration results, we reconstruct the Stokes vector from the obtained spectrum using the presented reconstruction method.

The reconstruction results of the polarization parameters of the target at three different viewing angles are given in Fig. 9. We use two methods to reconstruct the Stokes vector, i.e., the traditional method, named "reference beam calibration technique" [17], and the new method presented in this paper. The errors caused by ringing in the reconstruction have been alleviated through apodization, a well-known technique [26]. When reconstructing the Stokes vector, first, the raw obtained spectrum is multiplied by the apodizing window, which falls to zero at the edges of the system's working wave band. In this paper, the apodizing window we use is the Hann window [26]. Then, the reconstruction of the Stokes vector is performed by using the presented reconstruction method. Lastly, the apodizing window is divided back out of the reconstructed Stokes vector. In the traditional method, the alignment errors, and the polarization effects and variations of the phase factors at different viewing angles are not considered. Through the comparison and analysis, we can find that the alignment errors of the PSIM module will cause the reconstruction errors of the Stokes vector at all the viewing angles, which must not be ignored in the polarimetric calibration and Stokes vector reconstruction. Furthermore, using the traditional method, the reconstruction errors increase significantly with the viewing angle increasing, while the reconstructed Stokes vectors almost overlap each other at different viewing angles using the presented method. This is because if the polarization effects and variations of the phase factors are ignored, their influences on the reconstruction will be more serious as the viewing angle increases. With the traditional method, the residual errors of $S_1(\sigma)/S_0(\sigma)$, $S_2(\sigma)/S_0(\sigma)$, and $S_3(\sigma)/S_0(\sigma)$ over the working wave band are less than 9.6×10^{-3}, 7.0×10^{-3}, and 9.1×10^{-4}, which are decreased to 7.0×10^{-4}, 8.1×10^{-4}, and 1.2×10^{-4}, respectively, by using the presented methods. The reconstruction accuracy of the Stokes vector is improved by approximately 1 order of magnitude. In addition, we use the errors of degree of polarization (DOP), given by $\text{DOP}(\sigma)=\sqrt{S_1^2(\sigma)+S_2^2(\sigma)+S_3^2(\sigma)}/S_0(\sigma)$, to analyze the reconstruction results, which are shown in Fig. 9(d). The errors of DOP(σ) over the working wave band are greater than 1% without the polarimetric calibration, which cannot meet the application requirement for the spectropolarimetry. By the presented polarimetric calibration and reconstruction methods, the errors of DOP(σ) achieve about 0.1% across the entire

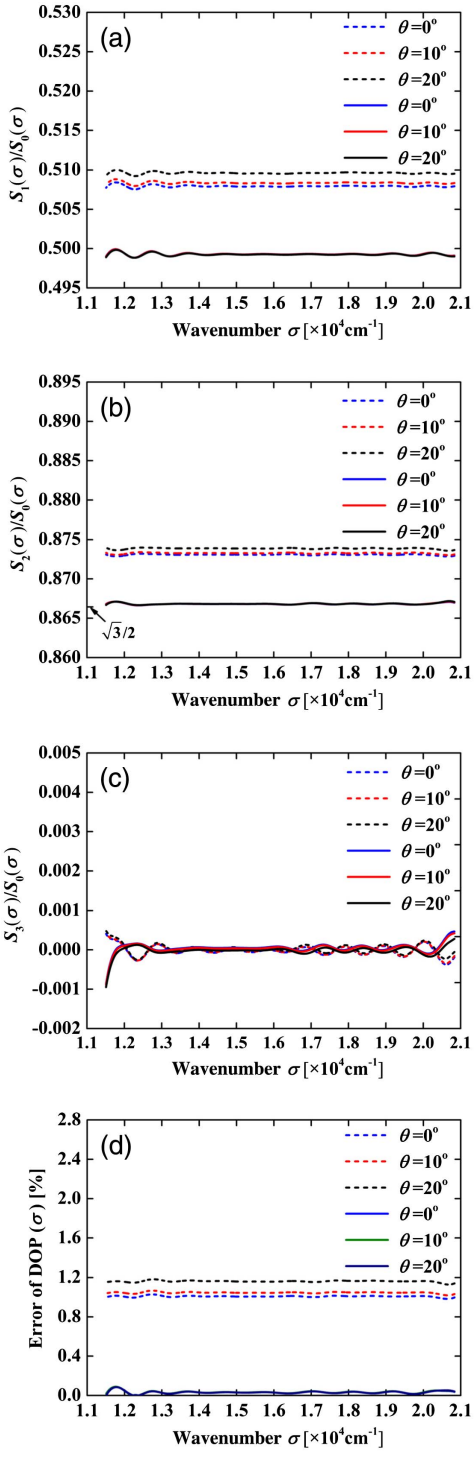

Fig. 9. Reconstruction results of the polarization parameters of the target with the traditional method and presented method. The dotted lines denote the results using the traditional method, while the solid lines denote the results using the presented method. (a) $S_1(\sigma)/S_0(\sigma)$, (b) $S_2(\sigma)/S_0(\sigma)$, (c) $S_3(\sigma)/S_0(\sigma)$, (d) error of DOP(σ). The reference values are $S_1(\sigma)/S_0(\sigma)=1/2$, $S_2(\sigma)/S_0(\sigma)=\sqrt{3}/2$, and $S_3(\sigma)/S_0(\sigma)=0$.

FOV. The results suggest that by using the presented method, the polarization information of the target can be obtained accurately across the entire FOV of the CDISP.

We should mention that the accuracy of the polarimetric calibration and reconstruction is affected by the spectral bandwidth. In the above simulations, the spectral bandwidth we use is 400 nm, i.e., the spectral range is 480–880 nm. To analyze the influence of the spectral bandwidth, we simulate the polarimetric calibration and reconstruction over 500–700 nm spectral range with other conditions remaining unchanged. The results show that the errors of DOP(σ) achieve about 0.21% across the entire FOV, which increases compared with the error of 0.1%, obtained over 480–880 nm spectral range. The reason is that the measurement accuracy of the channeled spectropolarimetry is strongly influenced by the cross talk of the channels, especially for the target light with narrow band spectrum, which is the inevitable defect of the channeled spectropolarimetry. When designing a fieldable CDISP, in order to decrease the influence of the cross talk of the channels, we generally optimize the thicknesses of the high-order retarders according to the working wave band. As a result, to improve the accuracy of the polarimetric calibration and reconstruction, we can use the maximum spectral range, which is designed for the fieldable CDISP, to perform the polarimetric calibration and reconstruction by the presented methods.

We also simulate the special condition that $\alpha_1 = 0$, and the results show that the presented polarimetric calibration and reconstruction methods are still effective in this condition. After analyzing the simulation results, we conclude that the measurement accuracy of the fieldable CDISP can be assured through the presented methods.

6. EXPERIMENTAL RESULTS

The configuration of the demonstration experiment is given in Fig. 10. The system to be calibrated consists of the fore-optics, PSIM module, relay optics, and a grating-based spectrometer (FieldSpec 3, Analytical Spectral Devices). The thicknesses of R_1, R_2, and R_3 are 1.8 mm, 3.6 mm, and 1.26 mm, respectively. The alignment errors of R_1 and R_2 are set to 0.5°. The aberrations of the system are corrected over 480–880 nm when the viewing angle of the fore-optics is less than 15°. A stabilized tungsten halogen lamp, an integrating sphere, a collimator, a circular aperture, and a rotatable polarizer, P_1, are used to generate the beams we need in the polarimetric calibration and reconstruction. The above devices are installed in a precision turntable and guide rail, which are used to adjust the beams to illuminate the system at different viewing angles. The spectrometer can obtain the modulated spectrum of the light passing through the system at different viewing angles in turn as the states of the precision turntable and guide rail are adjusted in the demonstration experiment.

When conducting the experiment, we first use the tungsten halogen lamp, integrating sphere, collimator, polarizer P_1, circular aperture, and collimator to generate a narrow and collimated beam to calibrate α_1 and α_2 with the auxiliary high-order retarder R_3. After that, to determine the parameters $\exp[i\varphi_1(\sigma,\theta)]$, $\exp[i\varphi_2(\sigma,\theta)]$, and $\delta_{\text{fore}}(\sigma,\theta)$, R_3 is removed, and the other devices are used to generate 0° and 45° linearly polarized beams to illuminate the system at different viewing angles and the responses are recorded, respectively. Lastly, the polarizer P_1, collimator, and circular aperture are removed, and the tungsten halogen lamp and integrating sphere are used to generate unpolarized light for determining $A(\sigma,\theta)$ and $D_{\text{fore}}(\sigma,\theta)$. Based on the above measurement data, the parameters can be calculated out by using the method described in Section 3. We provide the magnitudes of the autocorrelation functions of the obtained spectrum when the 0° and 45° linearly polarized reference beams are shined on the system at the viewing angle of 15°, which are shown in Fig. 11. We can find that the desired channels are separated from one another and their distributions are consistent with the simulation results, which further validate the feasibility of the presented polarimetric calibration method.

The Stokes vector of the target light is then reconstructed by using the determination results of the parameters. Figure 12 gives the reconstruction results through the two methods, i.e., the traditional method [17] and the method presented in this paper. The Stokes vector of the target light remains stable and uniform in the laboratory experiment. The reconstructed results using the traditional method indicate that the reconstruction errors become larger with the viewing angle increasing, which is caused by the polarization effects of the system and variations of the phase factors. In addition, the reconstructed results deviate from the reference values due

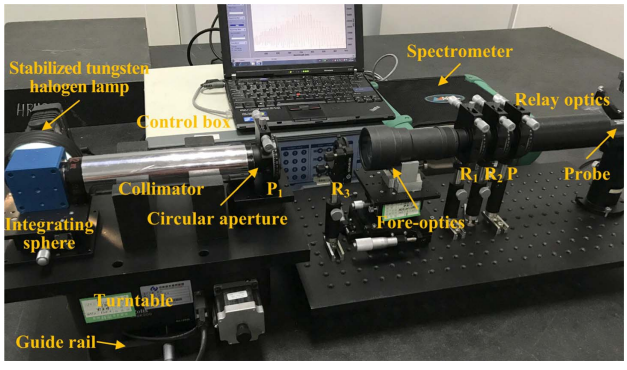

Fig. 10. Photograph of the configuration of the demonstration experiment. The high-order retarders, R_1, R_2, and R_3, and the polarizers, P_1 and P, are installed in precision adjusting racks.

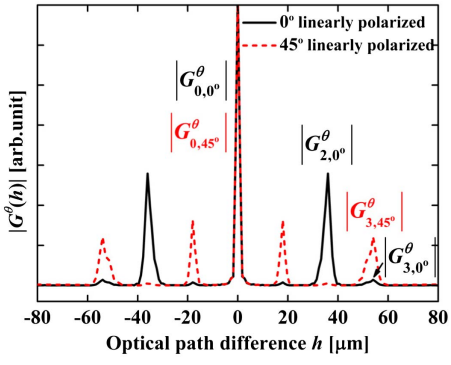

Fig. 11. Magnitudes of the autocorrelation functions when the 0° and 45° linearly polarized reference beams are shined on the system at the viewing angle of 15°.

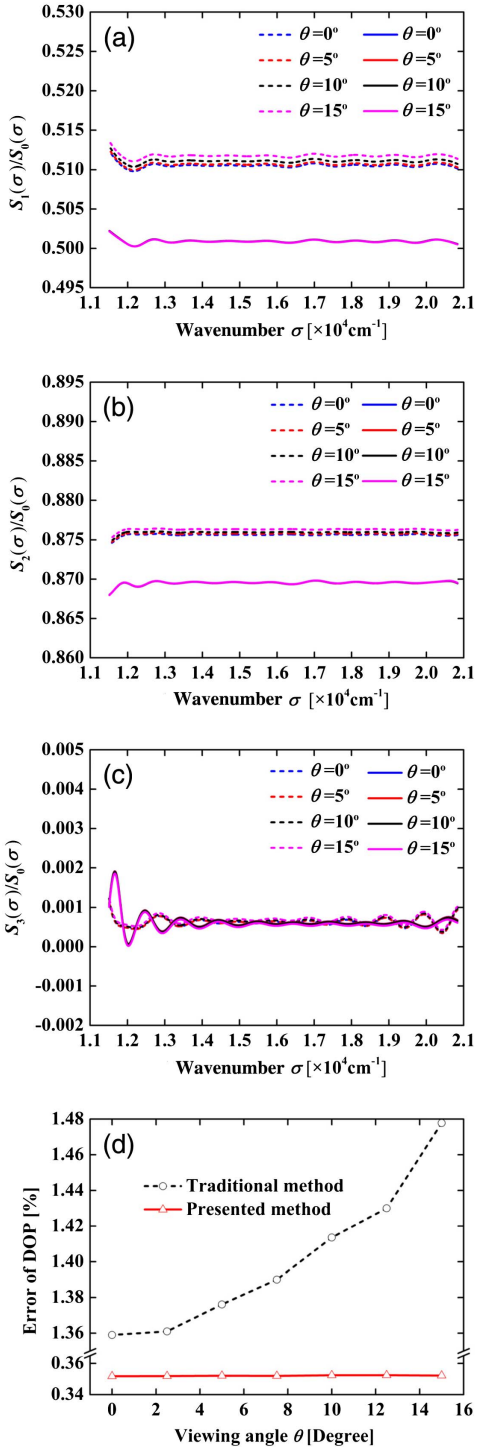

Fig. 12. Reconstruction results through the traditional method and presented method. The dotted lines denote the results using the traditional method, while the solid lines denote the results using the presented method. (a) $S_1(\sigma)/S_0(\sigma)$, (b) $S_2(\sigma)/S_0(\sigma)$, (c) $S_3(\sigma)/S_0(\sigma)$, (d) error of DOP(σ) in the selected wavenumber of $\sigma = 16969$ cm^{-1}. The reference values are $S_1(\sigma)/S_0(\sigma) = 1/2$, $S_2(\sigma)/S_0(\sigma) = \sqrt{3}/2$, and $S_3(\sigma)/S_0(\sigma) = 0$.

to ignoring the alignment errors of the PSIM module. However, similar to the simulation results, the reconstructed Stokes vectors at different viewing angles are almost overlapping each other by using the presented method, and the residual errors of $S_1(\sigma)/S_0(\sigma)$, $S_2(\sigma)/S_0(\sigma)$, and $S_3(\sigma)/S_0(\sigma)$ are less than 2.2×10^{-3}, 3.8×10^{-3}, and 1.8×10^{-3}, respectively. Figure 12(d) shows that the errors of DOP(σ) in a fixed wavenumber obtained by using the presented method do not change with the viewing angles significantly, and they achieve about 0.35% at all the viewing angles. From the reconstruction results, we can conclude that by using the presented polarimetric calibration and reconstruction methods, the influences of the polarization effects of the system, variations of the phase factors, and alignment errors of the PSIM module are reduced effectively, and Stokes vectors of the target light are obtained accurately at different viewing angles. After analysis, we think that the reasons why the experimental reconstruction errors are larger compared with the simulation results are because of the thickness errors of the high-order retarders, noise, stray light, and other environmental factors [23]. Noteworthy is that the reconstructed errors increase at the edges of the wave band due to the ringing, which is inevitable for the channeled spectropolarimetry [26]. To overcome this limitation, we can design and calibrate the system over a wider spectral range than necessary for the final application and truncate the edges of the reconstructed Stokes vector spectrum.

The experimental results indicate that the presented polarimetric calibration and reconstruction methods are effective for improving the reconstruction accuracy of the Stokes vector of the target light. For the system with a wider FOV or smaller F-number, the influences of the polarization effects of the optical system and variable phase factors of the high-order retarders will be more obvious. In this case, the presented methods can play a greater role in improving the measurement accuracy, which is significant for the quantitative-grade application of the fieldable CDISP.

7. CONCLUSION

This paper presents methods of polarimetric calibration and reconstruction for the fieldable CDISP. We first derive the theoretical model for the polarimetric calibration. Before calibrating the phase factors of the high-order retarders, R_1 and R_2, we quantitatively analyze the rules that the phase factors of R_1 and R_2 change with the incident angle, which show that the phase factor of R_1 changes obviously with the viewing angle while the phase factor of R_2 can be assumed to be a constant in the fixed wavenumber across the entire FOV of the fieldable CDISP. Based on the derived theoretical model and analysis results, we determine the exact values of the phase factor of R_2 at the central FOV and alignment errors of the PSIM module. Furthermore, the polarization effects of the fore-optics, polarization radiative transfer coefficients of the system, and phase factors of R_1 at different viewing angles are considered and determined independently to improve the calibration accuracy. In the polarimetric calibration, we use the beam that provides $S_1(\sigma) \neq 0$ and $S_2(\sigma) \neq 0$ or $S_3(\sigma) \neq 0$, 0° and 45° linearly polarized beams, and unpolarized beam as the reference light source, respectively, to determine the parameters need to be calibrated. By using the polarimetric calibration results, we can accurately reconstruct the Stokes vector of the target across the entire FOV of the fieldable CDISP through the presented

reconstruction method. Simulation and experimental results validate that the parameters need to be calibrated can be determined accurately, and the reconstruction accuracy of the Stokes vector at each viewing angle is improved because the influences of the parameters are effectively reduced. As a result, the presented polarimetric calibration and reconstruction methods can be used to improve the measurement accuracy of the fieldable CDISP.

Funding. National Natural Science Foundation of China (NSFC) (61505199); National High Technology Research & Development Program of China (2011AA12A103).

REFERENCES

1. C. Zhang, Q. Li, T. Yan, T. Mu, and Y. Wei, "High throughput static channeled interference imaging spectropolarimeter based on a Savart polariscope," Opt. Express **24**, 23314–23332 (2016).
2. T. Mu, S. Pacheco, Z. Chen, C. Zhang, and R. Liang, "Snapshot linear-Stokes imaging spectropolarimeter using division-of-focal-plane polarimetry and integral field spectroscopy," Sci. Rep. **7**, 42115 (2017).
3. W. Groner, J. W. Winkelman, A. G. Harris, C. Ince, G. J. Bouma, K. Messmer, and R. G. Nadeau, "Orthogonal polarization spectral imaging: a new method for study of the microcirculation," Nat. Med. **5**, 1209–1212 (1999).
4. S. H. Jones, F. J. Iannarilli, and P. L. Kebabian, "Realization of quantitative-grade fieldable snapshot imaging spectropolarimeter," Opt. Express **12**, 6559–6573 (2004).
5. D. J. Diner, R. A. Chipman, N. Beaudry, B. Cairns, L. D. Food, S. A. Macenka, T. J. Cunningham, S. Seshadri, and C. Keller, "An integrated multiangle, multispectral, and polarimetric imaging concept for aerosol remote sensing from space," Proc. SPIE **5659**, 88–96 (2005).
6. M. Dubreuil, S. Rivet, B. L. Jeune, and L. Dupont, "Time-resolved switching analysis of a ferroelectric liquid crystal by snapshot Mueller matrix polarimetry," Opt. Lett. **35**, 1019–1021 (2010).
7. R. S. Gurjar, V. Backman, L. T. Perelman, I. Georgakoudi, K. Badizadegan, I. Itzkan, R. R. Dasari, and M. S. Feld, "Imaging human epithelial properties with polarized light-scattering spectroscopy," Nat. Med. **7**, 1245–1248 (2001).
8. J. S. Tyo, D. L. Goldstein, D. B. Chenault, and J. A. Shaw, "Review of passive imaging polarimetry for remote sensing applications," Appl. Opt. **45**, 5453–5469 (2006).
9. J. Li, J. Zhu, and H. Wu, "Compact static Fourier transform imaging spectropolarimeter based on channeled polarimetry," Opt. Lett. **35**, 3784–3786 (2010).
10. K. Oka and T. Kato, "Spectroscopic polarimetry with a channeled spectrum," Opt. Lett. **24**, 1475–1477 (1999).
11. F. J. Iannarilli, S. H. Jones, H. E. Scott, and P. Kebabian, "Polarimetric-spectral intensity modulation (P-SIM): enabling simultaneous hyperspectral and polarimetric imaging," Proc. SPIE **3698**, 474–1477 (1999).
12. S. H. Jones, F. J. Iannarilli, C. Hostetler, B. Cairns, A. Cook, J. Hair, D. Harper, Y. Hu, and D. Flittner, "Preliminary airborne measurement results from the Hyperspectral Polarimeter for Aerosol Retrievals (HySPAR)," in *NASA Earth Science Technology Conference Proceedings* (2006), pp. 1–6.
13. J. S. Tyo and T. S. Turner, "Variable-retardance, Fourier-transform imaging spectropolarimeters for visible spectrum remote sensing," Appl. Opt. **40**, 1450–1458 (2001).
14. R. W. Aumiller, C. Vandervlugt, E. L. Dereniak, R. Sampson, and R. W. McMillan, "Snapshot imaging spectropolarimetry in the visible and infrared," Proc. SPIE **6972**, 69720D (2008).
15. N. Hagen, E. L. Dereniak, and D. T. Sass, "Visible snapshot imaging spectro-polarimeter," Proc. SPIE **5888**, 588810 (2005).
16. D. S. Sabatke, A. M. Locke, E. L. Dereniak, and R. W. McMillan, "Linear calibration and reconstruction techniques for channeled spectropolarimetry," Opt. Express **11**, 2940–2952 (2003).
17. A. Taniguchi, K. Oka, H. Okabe, and M. Hayakawa, "Stabilization of a channeled spectropolarimeter by self-calibration," Opt. Lett. **31**, 3279–3281 (2006).
18. T. Bret-Dibat, Y. Andre, and J. M. Laherrere, "Pre-flight calibration of the POLDER instrument," Proc. SPIE **2553**, 218–231 (1995).
19. R. A. Chipman, "Mueller matrices," in *Handbook of Optics*, M. Bass, ed. (McGraw-Hill, 1995), Chap. 14.
20. R. A. Chipman, "Polarization ray tracing," Proc. SPIE **766**, 61–68 (1987).
21. W. He, Y. Fu, Y. Zheng, L. Zhang, J. Wang, Z. Liu, and J. Zheng, "Polarization properties of a corner-cube retroreflector with three-dimensional polarization ray-tracing calculus," Appl. Opt. **52**, 4527–4535 (2013).
22. R. A. Chipman, "Polarization analysis of optical systems," Opt. Eng. **28**, 280290 (1989).
23. B. Yang, X. Ju, C. Yan, and J. Zhang, "Alignment errors calibration for a channeled spectropolarimeter," Opt. Express **24**, 28923–28935 (2016).
24. J. Dong and Y. Li, "Analysis and optimization approaches for wide-viewing-angle $\lambda/4$ plate in polarimetry for immersion lithography," J. Vac. Sci. Technol. B **31**, 011602 (2013).
25. R. A. Chipman, "Polarizer," in *Handbook of Optics*, M. Bass, ed. (McGraw-Hill, 1995), Chap. 13.
26. D. S. Sabatke, "Snapshot spectropolarimetry," Ph.D. dissertation (The University of Arizona, 2002).